Unveiling the Interfacial Effects for Enhanced Hydrogen Evolution Reaction on MoS$_2$/WTe$_2$ Hybrid Structures

Yu Zhou, Joshua V. Pondick, Jose Luis Silva, John M. Woods, David J. Hynek, Grace Matthews, Xin Shen, Qingliang Feng, Wen Liu, Zhixing Lu, Zhixiu Liang, Barbara Brena, Zhao Cai, Min Wu, Liying Jiao, Shu Hu, Hailiang Wang, Carlos Moyses Araujo, and Judy J. Cha*

Using the MoS$_2$-WTe$_2$ heterostructure as a model system combined with electrochemical microreactors and density function theory calculations, it is shown that heterostructured contacts enhance the hydrogen evolution reaction (HER) activity of monolayer MoS$_2$. Two possible mechanisms are suggested to explain this enhancement: efficient charge injection through large-area heterojunctions between MoS$_2$ and WTe$_2$ and effective screening of mirror charges due to the semimetallic nature of WTe$_2$. The dielectric screening effect is proven minor, probed by measuring the HER activity of monolayer MoS$_2$ on various support substrates with dielectric constants ranging from 4 to 300. Thus, the enhanced HER is attributed to the increased charge injection into MoS$_2$ through large-area heterojunctions. Based on this understanding, a MoS$_2$/WTe$_2$ hybrid catalyst is fabricated with an HER overpotential of −140 mV at 10 mA cm^{-2}, a Tafel slope of 40 mV dec^{-1}, and long stability. These results demonstrate the importance of interfacial design in transition metal dichalcogenide HER catalysts. The microreactor platform presents an unambiguous approach to probe interfacial effects in various electrocatalytic reactions.

1. Introduction

For the hydrogen evolution reaction (HER), the Sabatier principle plots the catalytic activity of solid-state catalysts as a function of the Gibbs free energy of hydrogen adsorption (ΔG_H) to a catalytic site and predicts optimal catalytic activity when ΔG_H is close to zero.[1] Many transition metal dichalcogenides (TMDs) have been investigated as potential electrocatalysts,[2–5] including MoS$_2$ that exhibits small ΔG_H,[6] which has led to extensive effort to use MoS$_2$ as an HER catalyst via nanostructuring,[7–9] strain-engineering,[10–15] and phase-engineering.[9,16,17] However, ΔG_H alone does not determine the overall HER activity; charge injection into MoS$_2$ has a large effect on catalytic efficiency.[18–20] Our previous work demonstrated that a Schottky barrier, a tunnel barrier for an electron at the interface between semiconducting MoS$_2$ and its conducting support, can suppress MoS$_2$ catalytic activity due to inefficient charge injection.[21] Additionally, for monolayer TMDs, the local environment can significantly modulate the electronic band structure[22–25] and electron transport dynamics.[26] For monolayer MoS$_2$, the immediately adjacent support can change multiple factors that affect HER, such as ΔG_H,[23] the doping level of MoS$_2$,[22] and the Schottky barrier height.[20,21] Indeed, several studies have shown varying HER activities by interfacing MoS$_2$ flakes with different

Dr. Y. Zhou, J. V. Pondick, J. M. Woods, D. J. Hynek, Prof. J. J. Cha
Department of Mechanical Engineering and Materials Science
Yale University
New Haven, CT 06511, USA
E-mail: judy.cha@yale.edu

Dr. Y. Zhou, J. V. Pondick, J. M. Woods, D. J. Hynek, X. Shen,
Dr. W. Liu, Z. Cai, M. Wu, Prof. S. Hu, Prof. H. Wang, Prof. J. J. Cha
Energy Sciences Institute
Yale West Campus, West Haven, CT 06525, USA

J. L. Silva, Prof. B. Brena, Prof. C. M. Araujo
Materials Theory Division
Department of Physics and Astronomy
Uppsala University
Uppsala 75120, Sweden

G. Matthews
Department of Materials Science and Engineering
North Carolina State University
Raleigh, NC 27695, USA

(iD) The ORCID identification number(s) for the author(s) of this article can be found under https://doi.org/10.1002/smll.201900078.

DOI: 10.1002/smll.201900078

X. Shen, Prof. S. Hu
Department of Chemical and Environmental Engineering
Yale University
New Haven, CT 06511, USA

Dr. Q. Feng
Shaanxi Key Laboratory of Optical Information Technology
School of Science
Northwestern Polytechnical University
Xi'an 710072, P. R. China

Dr. W. Liu, Z. Cai, M. Wu, Prof. H. Wang
Department of Chemistry
Yale University
New Haven, CT 06511, USA

Z. Lu, Prof. L. Jiao
Department of Chemistry
Tsinghua University
Beijing 10084, P. R. China

Dr. Z. Liang
Department of Chemistry
Brookhaven National Laboratory
Upton, NY 11973, USA

ADVANCED
SCIENCE NEWS
www.advancedsciencenews.com

NANO · MICRO
small
www.small-journal.com

supports.[24,26–29] Our previous results also showed that a graphene heterostructured contact (MoS_2/graphene heterostructure) yielded a 100 mV decrease in overpotential at 10 mA cm^{-2} as compared to graphene edge contacts.[21] Thus, establishing a clear understanding of precisely what effects the interface has on modulating the HER activities of MoS_2 is critical.[24,26–28]

Herein, we report the role of the interface on the catalytic performance of monolayer MoS_2 using semimetallic WTe_2 as a support. We use MoS_2-WTe_2 heterostructure nanodevices as microreactors to perform electrochemical characterization of the HER. The microreactor simplifies the catalytic system, allowing us to isolate the effects of ΔG_H, Schottky barriers, and the interface on HER activities. Results from the microreactors show significantly improved HER activities from the MoS_2-WTe_2 heterostructures, while the Schottky barrier and $|\Delta G_H|$ obtained from density function theory (DFT) calculations remain unaffected. To explain the improved HER, we examine the possibility of charge screening by semimetallic WTe_2 by measuring the catalytic efficiency of MoS_2 on insulating substrates with varying dielectric constants. We show that increasing the dielectric constant of the substrate decreases the catalytic activity. However, any effect due to the substrate is drastically overpowered by the presence of the contact resistance that affects charge injection. Thus, the improved catalytic efficiency is attributed to the improved electrical coupling in the MoS_2-WTe_2 heterostructure due to the large contact area and shorter electron transport length to the catalytic site. Based on our microreactor studies, we synthesized MoS_2/WTe_2 nanostructure hybrids with intimate contact between the two materials to optimize the interfacial charge transfer. The hybrid catalysts show an onset potential of ≈−50 mV, a Tafel slope of 40 mV dec^{-1}, and an overpotential of −140 mV at 10 mA cm^{-2}. Our results show that the insights gained from microreactor studies are important for optimal catalyst design.

2. Results and Discussion

Figure 1a shows a schematic of the band alignment of a heterostructure consisting of a monolayer MoS_2 in the semiconducting 2H phase and monolayer WTe_2 in the metallic T_d phase.[30] The work functions of monolayer MoS_2 and WTe_2 are 4.36 and 4.5 eV, respectively.[31–33] The relatively close Fermi level alignment between MoS_2 and WTe_2 leads to a lower Schottky barrier at the MoS_2-WTe_2 interface, compared to an interface between MoS_2 and common metal electrodes.[21] A lower Schottky barrier can improve HER activity by promoting efficient electron injection at the interface.[20,21] Figure 1b illustrates the microreactor fabricated for HER measurements. A small H_2SO_4 droplet serves as the electrolyte and a polymethyl methacrylate (PMMA) window is opened by electron-beam lithography to expose specific regions of MoS_2. The rest of the sample is covered with the PMMA layer to ensure that HER occurs only in the exposed regions. An Ag/AgCl reference electrode and a graphite counter electrode are used with linear sweep voltammetry at 5 mV s^{-1} to obtain polarization curves.

Three distinct microreactors were measured for comparison: basal-plane exposed MoS_2 with a WTe_2 contact (Figure 1c), edge-exposed MoS_2 with a WTe_2 contact (Figure 1d), and a basal-plane exposed MoS_2-WTe_2 heterostructure (Figure 1e). The MoS_2-WTe_2

heterostructure was constructed by stacking a chemical vapor deposited (CVD) monolayer MoS_2 flake on a mechanically exfoliated WTe_2 flake. Since we previously report that WTe_2 is catalytically active for the HER,[21] we ensured that only MoS_2 was exposed to the electrolyte during the measurement of the heterostructured devices. Comparison between the devices allows us to isolate the effect of the interface from the effect of the Schottky barrier. Figure 1f shows the polarization curves of the three cases, shown without ohmic drop (iR) compensation to study the role of interfacial effects on HER. Polarization curves of the basal- and edge-exposed MoS_2 with gold contact are also shown, which show no observable HER catalytic activity at low voltage range due to the high Schottky barrier between gold and MoS_2.[21] In contrast, the basal- and edge-exposed MoS_2 with WTe_2 contacts show comparable HER activities with an overpotential of ≈−270 mV at a current density of 10 mA cm^{-2}. Surprisingly, the basal-plane exposed MoS_2-WTe_2 heterostructure shows the best HER activity with an overpotential of ≈−150 mV at a current density of 10 mA cm^{-2}. Several microreactor devices were measured to confirm the observed trend (Figure 1g). The MoS_2-WTe_2 heterostructure consistently shows lower overpotentials (−135 ± 5 mV) than MoS_2 with the WTe_2 contact (−255 ± 15 mV) at 10 mA cm^{-2}.

The microreactor studies show two distinct effects. First is the improved HER using a WTe_2 contact instead of a gold contact. Second is the improved HER for the MoS_2-WTe_2 heterostructure compared to the WTe_2 contact case. We carry out DFT calculations to understand the two improvements (calculation details in the Experimental Section and in our previous report[21]). The calculated Schottky barrier heights are 0.25 eV for a 2H-MoS_2 monolayer on a T_d-WTe_2 monolayer and 0.61 eV for a 2H-MoS_2 monolayer on Au (111) (Figure S1, Supporting Information). Thus, the improved HER using the WTe_2 contact is due to a lower Schottky barrier between MoS_2 and WTe_2 than between MoS_2 and gold. However, the additional improvement in HER for the heterostructure compared to the WTe_2 contact case cannot be explained by the Schottky barrier, which is the same for both cases as the MoS_2-WTe_2 interface is identical.

Three factors may contribute to the improved HER activity of the heterostructure: change in ΔG_H of MoS_2 due to the underlying WTe_2, suppression of mirror charge formation as MoS_2 is sitting on semimetallic WTe_2 instead of insulating SiO_2, or enhanced charge injection due to the increased contact area of the heterointerface and shorter electron transport length. We consider the effect of ΔG_H first. Because our microreactors compare basal plane activities, we calculate only the basal plane ΔG_H. Our measured HER activities are likely from S-vacancies, which are catalytically active on the MoS_2 basal plane.[13,20,34] This is reflected in comparable overpotentials between the edge-exposed and basal plane-exposed MoS_2 device studies (Figure 1g). For the calculated values of ΔG_H shown in **Figure 2**a, we arbitrarily assume a S-vacancy concentration of 1.25% in the MoS_2 monolayer. Comparing the two systems (freestanding MoS_2 monolayer and MoS_2-WTe_2 heterostructure) with the same level of S-vacancies, the absolute value of the calculated ΔG_H is comparable for the two cases, 47 meV versus −40 meV, suggesting that ΔG_H is not affected by interfacing MoS_2 with WTe_2. We have also carried out calculations of the ΔG_H for the two cases with no S-vacancies, which shows negligible changes in ΔG_H by WTe_2 (Figure S2, Supporting Information).
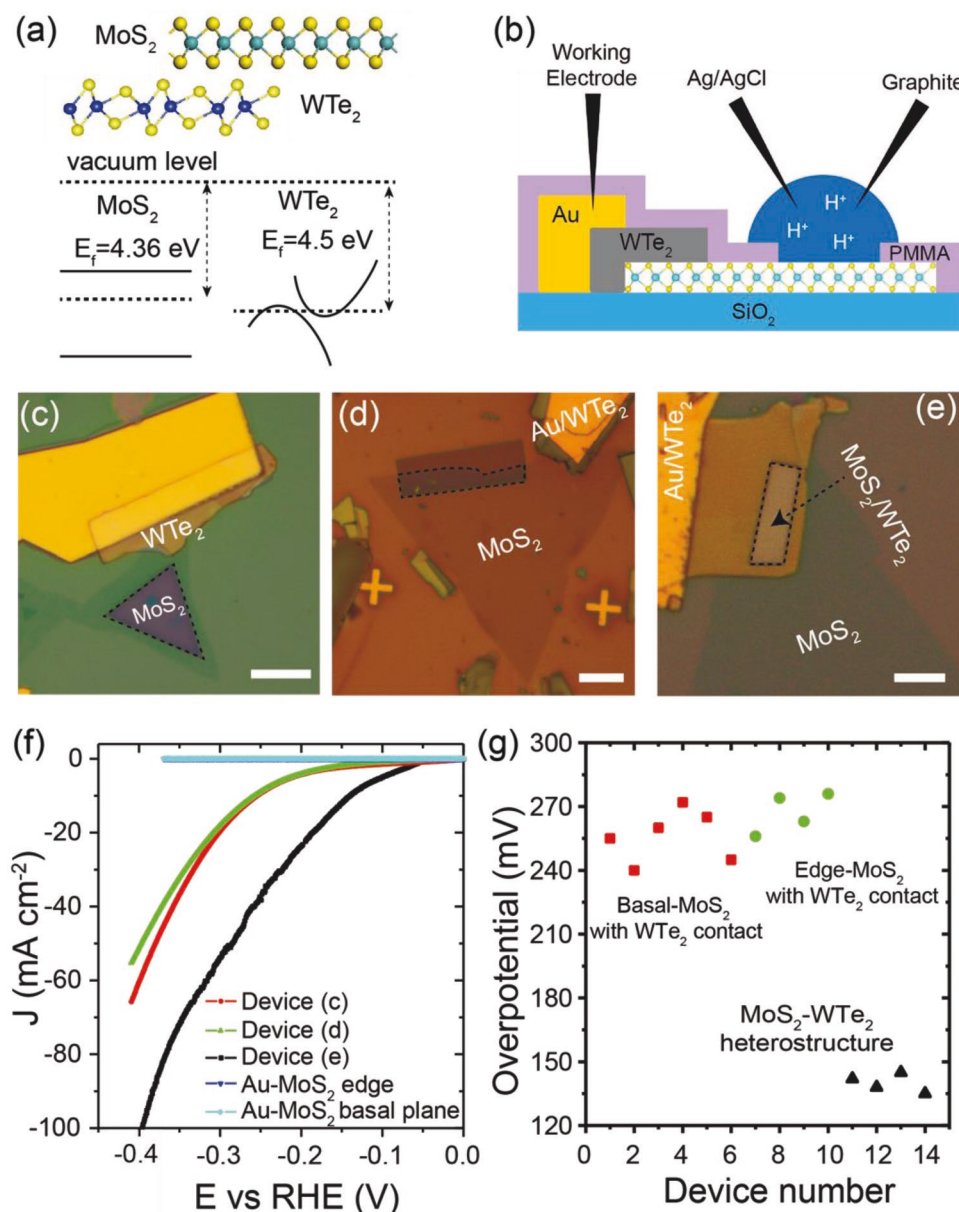
Figure 1. WTe$_2$-MoS$_2$ electrochemical microreactors. a) Schematic illustration of the MoS$_2$-WTe$_2$ heterostructure and band alignment at the MoS$_2$-WTe$_2$ interface. b) Cross-sectional schematic view of an electrochemical microreactor. Here, the basal plane of MoS$_2$ is exposed for HER with a WTe$_2$ contact. Optical images of WTe$_2$ contacted single layer MoS$_2$ microreactors with c) basal plane exposed and d) edge exposed. e) Basal-plane exposed MoS$_2$-WTe$_2$ heterostructure. For the microreactor measurements, except at the exposed window regions, the rest of the sample is covered with a PMMA layer. The black dashed lines indicate the exposed electrochemically active areas; scale bar, 10 µm. f) Typical polarization curves of the three cases in (c)–(e). g) Summary of the measured overpotentials for multiple devices for the three cases in (c)–(e) at 10 mA cm^{-2}.

The second possibility to explain the improved HER is suppression of mirror charge formation by semimetallic WTe$_2$. During the HER, electrons are depleted from MoS$_2$ to reduce protons to form hydrogen, and the resulting holes must be filled quickly to achieve high catalytic activities. For the microreactors in which the monolayer MoS$_2$ is placed on SiO$_2$, it is possible that mirror charges form near the MoS$_2$/SiO$_2$ interface to compensate for the holes in MoS$_2$ (Figure 2b). The holes could get stabilized by the mirror charges, impeding the rate of electron replenishment in MoS$_2$ monolayer. The hypothesis of

mirror charge formation and its potential impact on the HER activity is corroborated by recent reports that show enhanced HER activity by increasing the electron concentration in MoS$_2$ by gating.[35,36] Additionally, modifying the dielectric constant of the substrate has been predicted to modify the bandgap,[25] and shown to change the exciton lifetime in monolayer MoS$_2$.[37] The hypothesized mirror charges can be suppressed by semimetallic WTe$_2$ that sits directly underneath the monolayer MoS$_2$ (Figure 2b). Lastly, the third hypothesis for the enhanced activity in heterostructures is simply that the increased contact
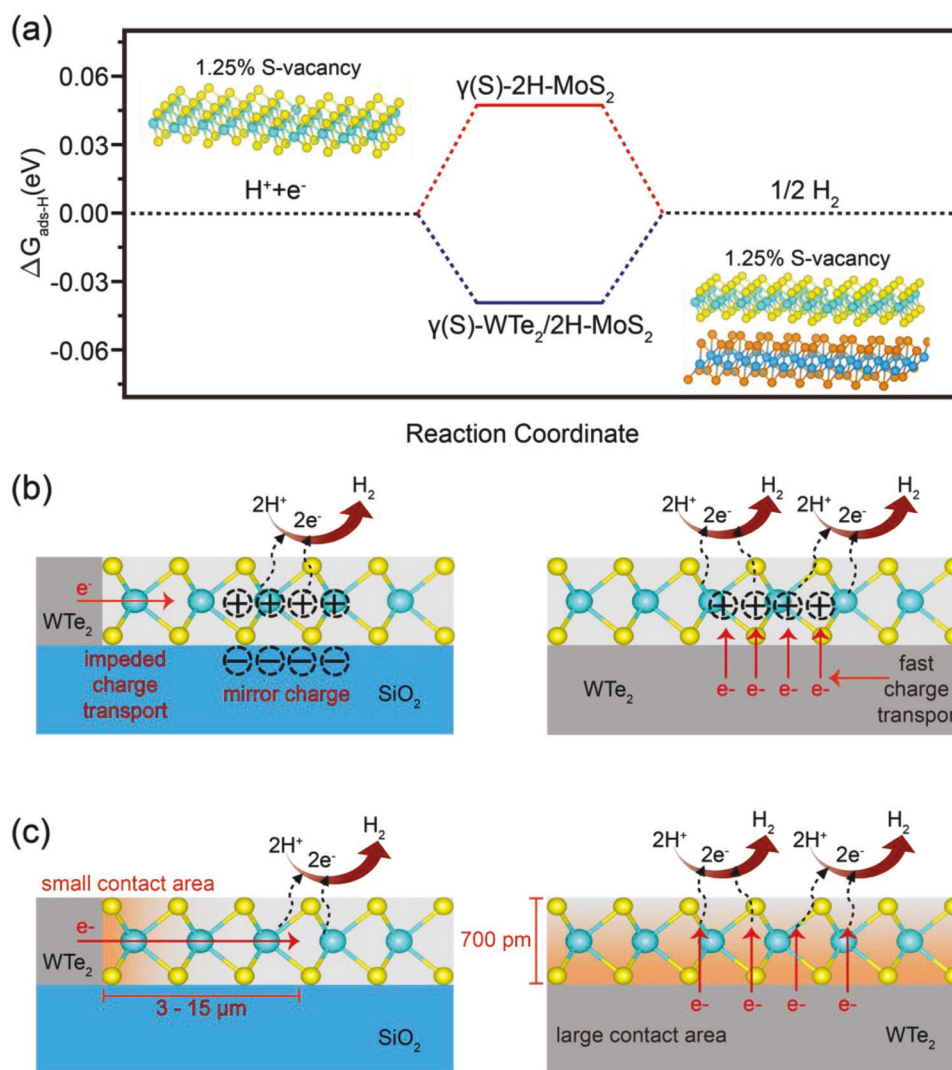
Figure 2. Interfacial effects on WTe$_2$-MoS$_2$ hybrids. a) Comparison of ΔG_H values of the S-vacancy site in the basal plane of the freestanding MoS$_2$ monolayer (0.047 eV) and of the MoS$_2$-WTe$_2$ heterostructure (−0.040 eV). We assume one S-vacancy out of 80 S atoms for 1.25% vacancy concentration. b) Schematics of image charge accumulation at SiO$_2$ versus WTe$_2$ interfaces and its influence on the charge transport dynamics on HER of a monolayer MoS$_2$. c) Schematics of WTe$_2$ edge-contacts versus heterostructure contacts to MoS$_2$. Contact area is represented by orange, while electron injection pathways from the contact to active site are shown as red arrows.

area due to the heterointerface enhances charge injection and reduces the electron pathway to the catalyst site for the MoS$_2$-WTe$_2$ heterostructure compared to the WTe$_2$ contact case, enhancing the HER kinetics (Figure 2c).

To test the second hypothesis that the formation of mirror charges impedes the HER activity, we measured the HER performance of monolayer MoS$_2$ microreactors using substrates with varying dielectric constants (κ). Thin layers ($\approx$10 nm) of Al$_2$O$_3$ ($\kappa = 9$), ZrO$_2$ ($\kappa = 25$), and TiO$_2$ ($\kappa = 80$) were deposited with atomic-layer deposition (ALD) onto SiO$_2$ ($\kappa = 4$) substrates (Figure S3, Supporting Information). Crystalline sapphire ($\kappa = 12$) and SrTiO$_3$ (STO, $\kappa = 300$) substrates were also used. To eliminate the effect of Schottky barriers, we used few-layer graphite flakes as side contacts to CVD-grown monolayer MoS$_2$ as we previously demonstrated that graphene-MoS$_2$ interfaces facilitate charge injection for the HER.[21] The graphite flakes

were connected to a larger gold pad as the functional working electrode. Due to poor adhesion of gold on dielectric substrates, we used a 10 nm Cr wetting layer for microreactors on SiO$_2$, Al$_2$O$_3$, and TiO$_2$, and a 10 nm Ni wetting layer for microreactors on STO, sapphire, and ZrO$_2$ to make contacts to graphite. Only the basal plane of MoS$_2$ was exposed for HER analysis as outlined schematically in **Figure 3**a, and in an optical image of a representative microreactor fabricated on STO (Figure 3b).

Representative polarization curves show that as the dielectric constant is increased, the HER activity gets worse (Figure 3c). The average overpotential at a current density of 10 mA cm^{-2} increases from −276 mV (SiO$_2$) to −347 mV (Al$_2$O$_3$) and −360 mV (TiO$_2$) using the Cr wetting layer, and it increases from −134 mV (sapphire) to −196 mV (ZrO$_2$) and −216 mV (STO) using the Ni wetting layer. The reduction in catalytic activity with increase in the dielectric constant of the substrate

ADVANCED
SCIENCE NEWS
www.advancedsciencenews.com

NANO · MICRO
small
www.small-journal.com
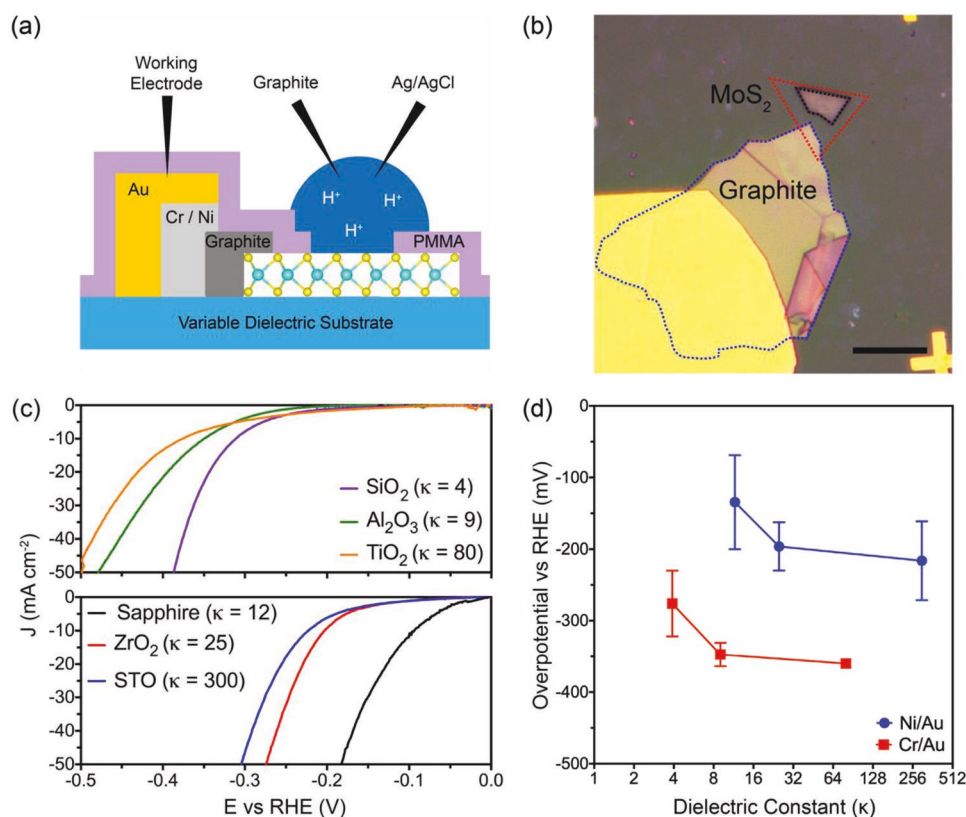
Figure 3. The effect of the dielectric substrate on HER activity. a) Cross-sectional schematic of the microreactors used to probe the effect of the dielectric substrate. Few-layer graphite is used to create edge contacts to MoS$_2$ and is contacted to gold using either a Cr or Ni wetting layer. b) Sample microreactor with basal-plane exposed MoS$_2$ supported on STO. Only the window (black dashed line) on the basal plane of the MoS$_2$ flake (red dashed line) is exposed to the electrolyte. The graphite contact (blue dashed line) is partially covered by Ni/Au; scale bar, 10 μm. c) Representative polarization curves from MoS$_2$ supported on dielectric substrates. The devices in the top plot have Cr-graphite contacts and the devices in the bottom plot have Ni-graphite contacts. d) Comparison of the overpotential required to reach a current density of 10 mA cm^{-2} as a function of dielectric constant of the support substrate (plotted on a log$_2$ scale) and graphite-metal interface.

supports the hypothesis of mirror charges impeding charge transport in MoS$_2$. However, the standard deviation in measured overpotentials is large (Figure 3d). The change in overpotential is also not dramatic: there is only an 82 mV difference in overpotential between sapphire and STO despite a $\Delta\kappa$ of 288. On the other hand, the catalytic efficiency is greatly enhanced using the Ni wetting layer as compared to the Cr wetting layer (Figures 3c,d). Despite having a κ of 300, STO-supported MoS$_2$ microreactors with graphite/Ni contacts showed lower overpotentials than MoS$_2$ reactors supported on SiO$_2$ (κ = 4) with graphite/Cr contacts.

The graphite contacts eliminate the effect of a Schottky barrier on charge injection to MoS$_2$, so the enhanced HER must originate from the interface between graphite and the wetting metal (Cr or Ni). Ni chemisorbs to graphene via hybridization between Ni d-orbitals and graphene π-orbitals, and can form low resistance contacts with graphene.[38,39] Experimentally determined contact resistances between graphene and Ni are lower than those with Au–Cr–graphene interfaces.[40,41] Therefore we conclude that the superior contact at the Ni-graphite interface facilitated charge injection, and led to improved HER activity over the Cr–graphite interface. The calculated Tafel slopes for all of the microreactors (Figure S4, Supporting Information) show no

distinct trend, indicating that neither the substrate nor the metal-graphene interface influenced the reaction pathway for the HER.

The HER measurements on various dielectric substrates suggest that the formation of mirror charges, our second hypothesis, cannot fully explain the improved HER of the MoS$_2$-WTe$_2$ heterostructure as the mirror charge effect is small. We attribute the HER enhancement to the third hypothesis: improved contact through the large-area heterointerface between WTe$_2$ and MoS$_2$ and shorter electron transport length (Figure 2c). For the MoS$_2$-WTe$_2$ heterostructure, the electron transport length to the catalytic sites is estimated to be ≈700 pm while it is 3–15 μm for the MoS$_2$ microreactor with a WTe$_2$ side contact. From the microreactor studies, we conclude that optimizing charge injection and reducing contact resistance within the electrochemical cell is key to achieving high-performing HER electrocatalysts.

The potential required to run the HER (E_{HER}) can be defined in terms of the standard reduction potential (E^0 = 0 V vs RHE) and the overpotential (η) via Equation (1)[42,43]

$$E_{HER} = E^0 + \eta \tag{1}$$

The overpotential describes the activation energy required for the reaction to proceed, and electrocatalysts work by reducing η.

ADVANCED
SCIENCE NEWS
www.advancedsciencenews.com

NANO · MICRO
small
www.small-journal.com

The reduced activation energy ($\eta_{catalyst}$) is determined by the thermodynamics of the interaction between the catalytic sites and hydrogen (ΔG_H). However, the experimentally determined η is typically larger than $\eta_{catalyst}$ due to additional energy barriers (E_B) such as the charge injection barriers discussed in this work and the ohmic drop (iR) through the electrochemical cell. Therefore, we can define η with Equation (2)

$$\eta = \eta_{catalyst} + E_B + iR \qquad (2)$$

We note that experimentally, E_B is usually corrected for by ohmic drop (iR) compensation; however, here we separate E_B to stress that this is a tunable barrier. By contrast, the iR is fixed by the resistance of the electrolyte and electrical connections in the measurement electronics.[42,43] Our heterostructured devices improve the catalytic efficiency by significantly reducing E_B to approach the thermodynamically predicted $\eta_{catalyst}$ of MoS$_2$.

Schottky barriers and charge injection are an issue for all semiconducting electrocatalysts, so the minimization of E_B can be applied more generally to other materials systems. Our results suggest that using low-Schottky barrier contacts or 2D support materials whose Fermi level is closely aligned with 2D semiconducting catalysts are promising strategies for reducing E_B. Recent advances in strain engineering of 2D TMDs have shown that their electronic band structure is sensitive to strain,[44–46] and could be used to tune the contact resistance at semiconductor–metal interfaces. Some work has demonstrated that strain engineering can also be used to improve the HER activity of TMDs by modifying ΔG_H.[10–15,47] Therefore, care must be taken to separate out the effects of strain on thermodynamics and charge injection. Although minimizing E_B is important for lowering η, further active site engineering will likely be necessary to tune the kinetics of the HER in order to achieve low Tafel slopes and high turn-over frequencies.

The improved HER of the MoS$_2$-WTe$_2$ heterostructures motivates us to synthesize MoS$_2$/WTe$_2$ hybrid catalysts as a proof-of-concept to demonstrate that insights gained from the microreactor studies can be applied to real materials systems although tellurium-based materials are expensive and thus impractical for commercial applications. Hybrid structures were synthesized solvothermally in N,N-dimethylformamide (DMF)/ hydrazine solvents. MoS$_2$ layers were grown directly on CVD-grown WTe$_2$ flakes using (NH$_4$)$_2$MoSO$_4$ as a precursor. This created a nanostructured catalyst with intimate contact between MoS$_2$ and WTe$_2$ to simulate the heterostructured devices. The microstructure of the MoS$_2$/WTe$_2$ hybrids was characterized by transmission electron microscopy (TEM). **Figure 4**a,b shows few-layer MoS$_2$ nanosheets intimately anchored on WTe$_2$ nanoflakes. High resolution TEM images show MoS$_2$ interlayer spacing of 0.62 nm (Figure 4b) and 0.27 nm (Figure S5, Supporting Information), suggesting that the MoS$_2$ layers are
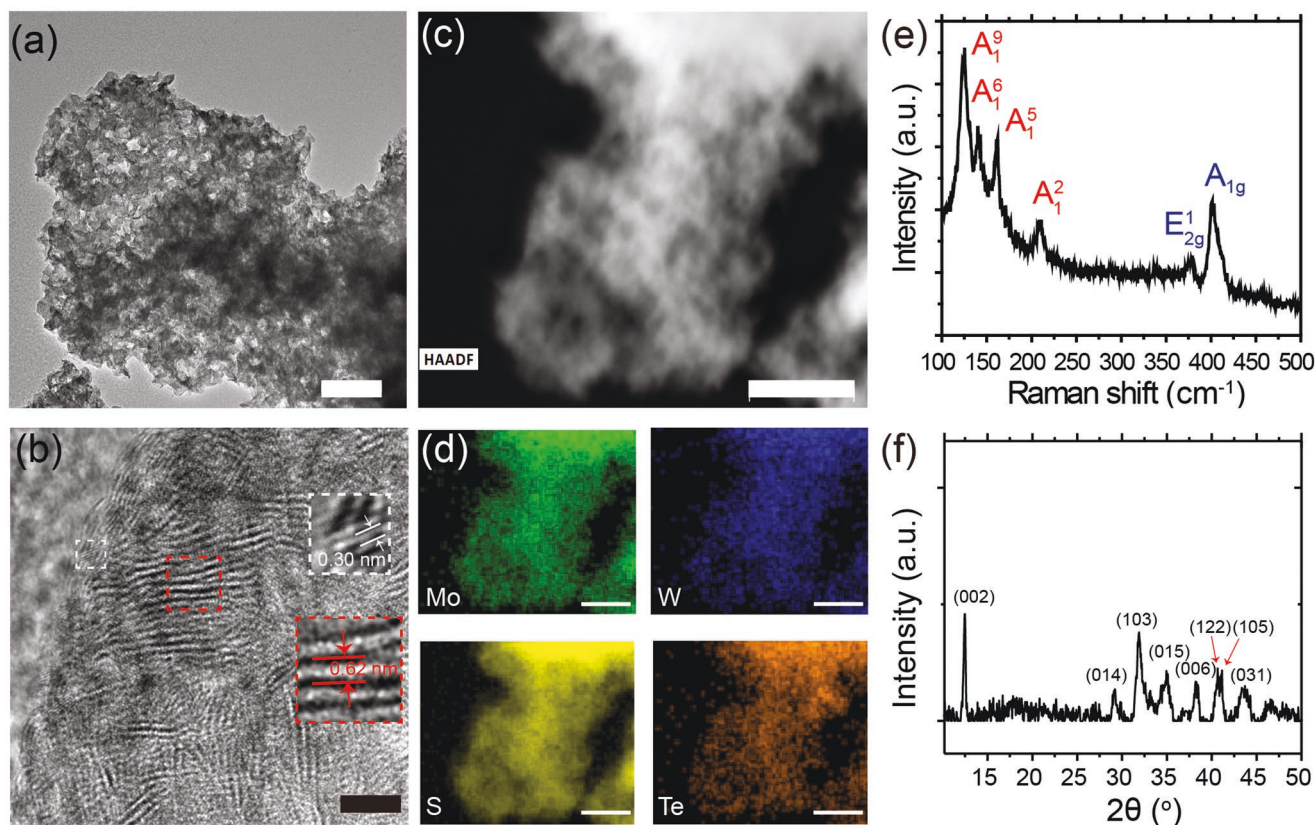
Figure 4. Structural characterization of MoS$_2$/WTe$_2$ hybrids. a) Low-magnification TEM image of a MoS$_2$/WTe$_2$ hybrid; scale bar, 100 nm. b) High-resolution TEM image; scale bar, 5 nm. Inset shows the lattice spacing of 0.30 and 0.62 nm, which correspond to the (020) plane of WTe$_2$ and (002) plane of MoS$_2$, respectively. c) HAADF STEM image of the hybrid; scale bar, 200 nm. d) STEM-EDX elemental mapping of the MoS$_2$/WTe$_2$ hybrid showing a homogeneous distribution of Mo (green), S (yellow), W (blue), and Te (orange); scale bar, 200 nm. e) Raman spectrum of the MoS$_2$/WTe$_2$ hybrid. Modes for both WTe$_2$ (red) and MoS$_2$ (blue) are identified. f) XRD pattern of the MoS$_2$/WTe$_2$ hybrid.

**ADVANCED
SCIENCE NEWS**
www.advancedsciencenews.com

NANO · MICRO
small
www.small-journal.com

oriented vertically as well as horizontally with respect to the WTe$_2$ flakes. Figure 4b and Figure S5 (Supporting Information) show the WTe$_2$ (020) plane spacing of 0.30 nm. Based on TEM analysis, ultrathin MoS$_2$ layers whose layer alignment is vertical to the WTe$_2$ flakes appear dominant over the horizontal layer alignment. Energy dispersive X-ray spectroscopy (EDX) mapping with high-angle annular dark field scanning TEM (HAADF STEM) shows that the MoS$_2$/WTe$_2$ hybrids have uniform distributions of Mo, W, S, and Te (Figures 4c,d, and Figure S6, Supporting Information). Raman spectroscopy was used to identify the chemical bonding vibrational modes of the hybrid catalyst. Six active Raman modes were observed at 120, 140, 161, 210, 383, and 407 cm^{-1}, which correspond to the WTe$_2$ out-of-plane A^9_1, A^6_1, A^5_1, and A^2_1 modes, and the MoS$_2$ in-plane E^1_{2g} and out-of-plane A_{1g} modes (Figure 4e).[30] The observed Raman modes exclude the possibility of alloy formations and doping effects between MoS$_2$ and WTe$_2$. Lastly, an X-ray diffraction (XRD) pattern was obtained to show distinct peaks that correspond to WTe$_2$ (Figure 4f). The absence of clear MoS$_2$ diffraction peaks suggests that the MoS$_2$ flakes are very small and perhaps partly amorphous.

The HER electrocatalytic activity of the MoS$_2$/WTe$_2$ hybrid was measured in a 0.5 M H$_2$SO$_4$ aqueous solution with conventional three electrode voltammetry using graphite and Ag/AgCl as counter and reference electrodes, respectively. The MoS$_2$/WTe$_2$ hybrid sample was drop-casted on a carbon fiber paper electrode with a mass loading of 1.2 mg cm^{-2}. For comparison, WTe$_2$ flakes only and MoS$_2$ nanosheets only samples were also prepared on a carbon fiber paper electrode with the same mass loading of 1.2 mg cm^{-2}.[48,49] The polarization curves are iR-corrected for the nanostructure samples. **Figure 5**a shows that the MoS$_2$/WTe$_2$ hybrid catalyst exhibits a substantially enhanced HER activity compared to the WTe$_2$ flakes and MoS$_2$ nanosheets case, with a low onset potential of −50 mV and an overpotential of −140 mV at a current density of 10 mA cm^{-2}. As a control, we show that the carbon-fiber paper shows no HER activity in this potential window (Figure S7, Supporting Information). We previously showed that the HER at MoS$_2$ is thermodynamically favored over WTe$_2$,[21] which is reflected in the better overpotential of the MoS$_2$ nanosheets over the CVD-grown WTe$_2$ (Figure 5a). Therefore, we attribute the enhanced HER performance of the MoS$_2$/WTe$_2$ hybrids to enhanced charge injection through the WTe$_2$ support into the MoS$_2$ nanosheets. The linear regions of the plots of ln(|J|) versus overpotential in Figure 5b were fitted to the Tafel equation. The Tafel slopes of the MoS$_2$/WTe$_2$ hybrid, WTe$_2$ flakes, and MoS$_2$ nanosheets are extracted to be ≈40, 66, and 112 mV dec^{-1}, respectively. In the low overpotential region, the Tafel slope for the Volmer, Heyrovsky, and Tafel reaction are ≈120, ≈40, and ≈30 mV dec^{-1}, respectively.[50,51] Thus, the Tafel slope of MoS$_2$/WTe$_2$ hybrids (40 mV dec^{-1}) suggests that the HER process is dominated by the Volmer–Heyrovsky mechanism.[26,50]

Electrochemical impedance spectroscopy (EIS) was carried out to better understand the reaction kinetics.[9] The impedance spectra of WTe$_2$ flakes, MoS$_2$ nanosheets, and the MoS$_2$/WTe$_2$ hybrids were obtained at −400 mV versus RHE. In the Nyquist plot (Figure 5c and the full scan in Figure S7, Supporting Information), only the MoS$_2$/WTe$_2$ hybrid shows a semicircle. The resistance of the MoS$_2$/WTe$_2$ hybrid catalyst is significantly

lower than those of WTe$_2$ flakes and MoS$_2$ nanosheets. The low series resistance (1.6 Ω) and charge transfer resistance (2 Ω) for the hybrid catalyst indicate high electrical conductivity of the semimetallic WTe$_2$ and low interfacial Schottky barrier at the MoS$_2$-WTe$_2$ interface,[26,52] which provides efficient charge injection for HER. Stability of the MoS$_2$/WTe$_2$ hybrid catalyst was checked by cycling the linear sweep voltammetry with no obvious degradation after 3000 cycles (Figure 5d).

We note that there are some key differences between our hybrid catalysts and the heterostructured microreactors. The reduced size and morphology of the hybrid nanoparticles (Figure 4) as compared to the heterostructured devices (Figure 1) indicates that the edge site density of the hybrid catalysts has likely been significantly increased. Unlike the heterostructured devices, where we can precisely define the active area with nanofabrication, the active area of the hybrid catalysts is estimated based on geometric area. Additionally, the crystal quality of the CVD-grown MoS$_2$ used in the microreactors is likely different from that of the crystals grown solvothermally for the hybrid catalysts. All of these factors can explain the differences between the performance of the heterostructured microreactors and the hybrid catalysts. However, the underlying mechanism of catalytic enhancement through the optimization of charge injection still applies to both systems, and explains the vast improvement in the performance MoS$_2$-WTe$_2$ heterostructures and hybrid HER catalysts. The hybrid catalysts demonstrate competitive performance as compared to other previously reported HER catalysts[3,4,42,43,53,54]; more importantly however, they demonstrate that the insights gained from microreactors can be applied to real catalyst systems.

3. Conclusion

In summary, the HER properties of a MoS$_2$-WTe$_2$ heterostructure were carefully studied using electrochemical microreactors and DFT calculations to highlight the role of the interface on HER. The MoS$_2$-WTe$_2$ interface enhances the charge injection due to a small Schottky barrier, improved contact due to the large-area heterointerface, and reduced electron transport pathways. Investigations of the effect of the substrate dielectric constant on HER activity demonstrate that bound mirror charges are potentially detrimental to catalysis; however, this effect is subtle. Based on understanding gained from the model microreactor system, a MoS$_2$/WTe$_2$ hybrid catalyst was fabricated to show a low overpotential of −140 mV at 10 mA cm^{-2}, a Tafel slope of 40 mV dec^{-1}, and long stability. These results demonstrate the importance of interface design in the TMD HER catalysts. The microreactor platform presents an unambiguous approach to probe interfacial effects in various electrocatalytic reactions, and insights gained with microreactors can be applied to the engineering of real catalyst systems.

4. Experimental Section

Synthesis of WTe$_2$ Flakes: WTe$_2$ source powder (0.55 g, 99.999%, American Elements) and I$_2$ (80 mg, 99.8%, Sigma-Aldrich) transport agent were used to grow WTe$_2$ bulk crystals via chemical vapor transport in a two-zone furnace.[31,55] A quartz tube loaded with the chemicals was

ADVANCED
SCIENCE NEWS
www.advancedsciencenews.com

NANO · MICRO
small
www.small-journal.com
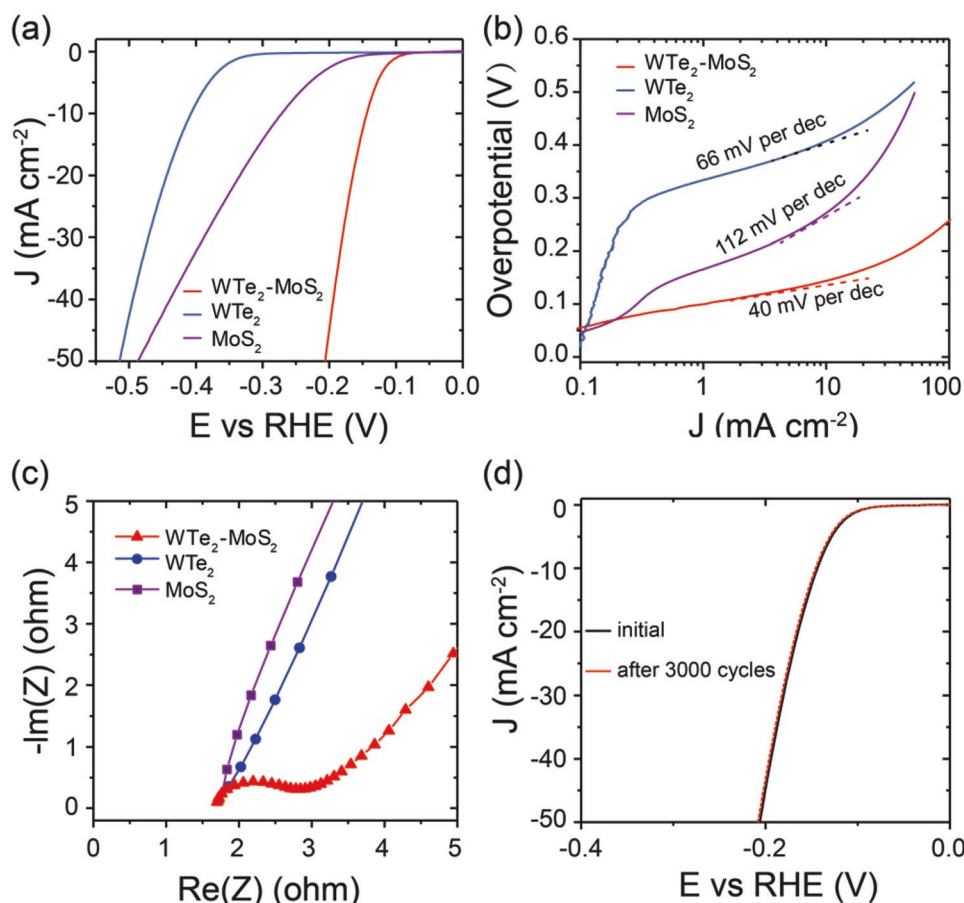
Figure 5. HER properties of MoS_2/WTe_2 hybrid catalyst. a) Polarization curves and b) corresponding Tafel plots of the MoS_2/WTe_2 hybrid catalysts, MoS_2 nanosheets, and WTe_2 flakes. c) Nyquist plots of the three samples. The full range is shown in Figure S7 (Supporting Information). d) Polarization curves show no obvious current density loss after 3000 cycles for the MoS_2/WTe_2 hybrid catalyst.

purged with argon gas 5–6 times and sealed under vacuum. The "cold" end was heated to 800 °C and the "hot" end with the source powder was heated to 950 °C in 6 h, and the temperature was maintained for 3 d. WTe_2 crystals were obtained at the "cold" end after natural cooling. Thin WTe_2 flakes were mechanically exfoliated onto SiO_2/Si substrates for manufacture of the heterostructure devices. WTe_2 was also synthesized via CVD on SiO_2 substrates using vaporized tellurium powder (99.997%, Sigma-Aldrich) to tellurize a W seed layer deposited with a magnetron sputtering system (AJA International) as described previously.[30]

Growth and Transfer of MoS_2 Flakes: Monolayer triangular MoS_2 flakes were grown on SiO_2/Si substrates in a single-zone furnace using CVD. MoO_3 (99.97%, Sigma-Aldrich) and sulfur powder (99.5%, Alfa Aesar) were used as growth precursors. For the heterostructure devices, the growth was conducted at 200 mTorr under 90 sccm of argon at 700 °C for 45 min as described previously.[56,57] The single-layer MoS_2 domain was transferred onto SiO_2/Si substrates with exfoliated WTe_2 to form MoS_2/WTe_2 heterostructures using a PMMA-mediated HF etching process. For the microreactors fabricated on various dielectric substrates, growth substrates for MoS_2 flakes were treated with hexamethylpararosaniline chloride (500 × 10^{-9} M aqueous solution, >90%, Sigma-Aldrich) and grown at atmospheric pressure under 20 sccm of argon at 700 °C for 5 min as described in our previous work.[58] The flakes were then spin-coated with cellulose acetate butyrate polymer (CAB, 12–15 wt% Acetyl/36–40 wt% Butyryl, $M_n \approx 30\,000$, Sigma-Aldrich) and transferred to prepatterned substrates using a water-mediated transfer process.[59]

Solvothermal Synthesis of MoS_2: Solvothermal synthesis of MoS_2 was carried out using ammonium tetrathiomolybdate (($NH_4)_2MoS_4$, 99.95%, Alfa Aesar) precursor with a hydrazine monohydrate ($NH_2NH_2 \cdot H_2O$, 99%,

Alfa Aesar) reducing agent in *N,N*-dimethylformamide (($CH_3)_2NCH$, 99.8%, Sigma Aldrich) solvent.[26] CVD-grown WTe_2 flakes were added to the solution as growth-substrates. The reagents were enclosed in an autoclave vessel and heated to 200 °C for 10 h, resulting in a hybrid structure of MoS_2 nanoparticles grown on WTe_2 support flakes.

Preparation of Dielectric Substrates: Substrates with a 300 nm layer of SiO_2 on Si (University Wafer), crystalline sapphire (Al_2O_3, (0001)-plane exposed, MTI Corporation), and crystalline strontium tin oxide ($SrTiO_3$, (100)-plane exposed, MTI Corporation) were patterned with Cr/Au (10 nm/100 nm) alignment marks. Substrates with varying dielectric constants were created via deposition of a thin layer of amorphous oxide onto prepatterned SiO_2 alignment substrates using an ALD system (Ultratech Fiji G2) with 30 sccm of Ar and 80 sccm of Ar plasma carrier gas. TiO_2 was prepared using 72 cycles of 0.25 s pulses of tetrakis(dimethylamido)titanium(IV) (TDMAT, 99.999%, Sigma-Aldrich), and 0.06 s pulses of water precursor, with the substrate heated to 150 °C and TDMAT heated to 75 °C. Al_2O_3 was prepared using 100 cycles of 0.06 s pulses of trimethylaluminum chloride (TMA, 99.999% Strem Chemicals), and 0.06 s pulses of water precursor, with the substrate heated to 150 °C. ZrO_2 was prepared using 150 cycles of 0.05 s pulses of tetrakis(dimethylamido)zirconium(IV) (TDMAZ, 99.99%, Strem Chemicals), and 0.4 s pulses of water precursor, with the substrate heated to 300 °C and TDMAZ heated to 75 °C.

Device Fabrication: The heterostructure devices were fabricated with transferred single-layer MoS_2 flakes that were partially covered by WTe_2 flakes. Standard electron beam lithography (EBL, Vistec EBPGRaith EBPG 5000+, ≈1000 nm PMMA resist) was used to pattern electrodes onto the WTe_2 and 100–200 nm gold contacts with a 10 nm Cr wetting

layer were deposited via thermal evaporation (MBraun MB-EcoVap). The dielectric devices were fabricated using a transfer stage. Briefly, thin graphite was tape-exfoliated from graphite flakes (NGS Naturgraphit GmbH) and then transferred onto PDMS (polydimethylsiloxane) placed on a glass slide. Target dielectric substrates with CAB-transferred MoS_2 flakes were placed on a transfer stage and the glass slide was lowered toward the substrate using a micromanipulator with the PDMS/graphite side face-down. Using an optical microscope, the thin graphite flakes were selectively placed on the corners of individual MoS_2 flakes, and then heated to 60 °C, causing the graphite to adhere to the MoS_2. Removal of the PDMS left graphite flakes contacting MoS_2. EBL was used to pattern electrodes onto the few-layer graphite and then 100 nm of Au with either a wetting layer of 10 nm Cr or 10 nm of Ni was thermally evaporated to create contacts. All microreactors were coated with another PMMA layer after creating gold contacts. A PMMA window to expose only the MoS_2 basal plane or edge was fabricated by a second EBL step. Before and after HER measurements, it is checked to ensure that the gold electrodes, WTe_2 contacts, and graphite contacts are well covered by the PMMA film.

Materials Characterization: ALD-grown oxide films were characterized using a monochromatic 1486.7 eV Al Kα X-ray source on a PHI VersaProbe II X-ray photoelectron spectrometer with a 0.47 eV system resolution. The energy scale was calibrated using Cu $2p_{3/2}$ (932.67 eV) and Au $4f_{7/2}$ (84.00 eV) peaks on a clean copper plate and clean gold foil. The spectra were normalized using the C 1s peak at 284.5 eV from adventitious carbon. Hybrid MoS_2/WTe_2 samples were characterized using Raman spectroscopy (532 nm laser, Horiba LabRAM HR Evolution Spectrometer), TEM/STEM (FEI Tecnai Osiris 200 kV TEM), and with XRD (Cu Kα 1.5406 Å source, Rigaku SmartLab XRD).

Electrochemical Measurements: Standard three-electrode voltammetry was used to measure the electrochemical properties of individual microreactors and hybrid materials. For microreactors, gold electrodes were used as the working electrode. The counter and reference electrodes were a sharp graphite rod and a home-made Ag/AgCl microelectrode, respectively. For the dielectric devices, a commercial Ag/AgCl reference electrode with a 450 µm tip was used (World Precision Inc.). The hybrid materials (0.8–1.2 mg cm^{-2} mass loading) were drop cast onto carbon fiber paper and dried fully. The carbon papers were then used as the working electrode to characterize the hybrid materials with graphite counter and Ag/AgCl reference electrodes. The electrochemical microreactors were measured in a small droplet of H_2SO_4 (0.5 M, oxygen free), while the hybrid systems were measured in a standard cell in H_2SO_4. For both microreactors and the hybrid system, linear sweep voltammetry was used to measure polarization curves at a scan rate of 5 mV s^{-1} from 0 to −500 mV versus the reversible hydrogen electrode using a Biological SP300 workstation. All potentials are converted according to E (versus RHE) = E (versus Ag/AgCl) + 0.290 V. The measured currents of microreactors were between 10^{-10} and 10^{-6} A. Current densities were obtained by normalizing the measured currents by the PMMA window surface area, which is exposed to the electrolyte solution. Impendence spectroscopy on MoS_2, WTe_2 and MoS_2/WTe_2 was conducted at a potential-static mode at −400 mV versus RHE with sinusoidal voltage of 10 mV amplitude and scanning frequency from 100 kHz to 5 mHz.

Computational Details: The plane wave[60] density-functional theory[61,62] was employed with the projected augmented wave method (PAW)[63] approach as implemented in Vienna Ab-initio Simulation Package (VASP).[64–66] The exchange and correlation interactions were treated with the generalized gradient approximation (GGA) within Perdew–Burke–Enzerhof (PBE).[67] For comparison, two heterostructures with exposed basal planes have been investigated, viz. T_d-WTe_2/2H-MoS_2 and Au(111)/MoS_2. A slab geometry of Au (111) with three layers was used. The stripes of WTe_2 and Au(111) were built under an absolute strain of 2.3% and 0.79%, respectively. Relaxations were performed to ensure the convergence of energies and forces in the range of 10^{-5} eV and 10^{-2} eV/Å. The Dumped van der Waals dispersive correction scheme DFT-D$_3$ developed by Grimme[68] was included to minimize residual charge fluctuations and the vacuum region was set to ≈15 Å. The plane

wave basis was set to 680 eV and the Brillouin zone was sampled with $2 \times 2 \times 1$ grid with the Monkhorst-Pack,[69] followed by static calculations with K-point of $6 \times 6 \times 1$ grid for both heterostructures. The Schottky barrier was estimated directly from the density of states (DOS) as the difference between the bottom of the conduction band (DOS projected on 2H-MoS_2 site) and the Fermi level (from the total DOS). The Gibbs free energy ΔG_{H*} of the adsorption of an intermediate hydrogen, on the basal plane, was also evaluated through Equation (3)

$$\Delta G_{H*} = E_{surf+H*} - E_{surf} - \frac{1}{2}E_{H_2^*} + \left(E_{ZPE}^{H*} - \frac{1}{2}E_{ZPE}^{H_2^*}\right) - T\Delta S_{H*} \quad (3)$$

where $E_{surf+H*}$ is the adsorption energy of the hydrogen onto a specific surface site, E_{surf} is the total energy of the surface without the hydrogen, $E_{H_2^*}$ indicates the gas phase energy of H_2^*, E_{ZPE}^{H*} and $E_{ZPE}^{H_2^*}$ are the zero point energies associated with the hydrogen adsorbed state and the hydrogen gas phase, respectively. Here, ΔS_{H*} is the entropy difference between the adsorbed hydrogen and the gas phase which can be approximated as the entropy of H_2^* at standard conditions $\Delta S_{H*} \cong -\frac{1}{2}S_{H_2^*}^0$. The zero point energies were determined through the calculation of the Hessian matrix and vibrational frequencies using the method of finite differences. In order to guarantee the harmonic limit in the calculation of the Hessian Matrix, the displacement for each ion was set to 0.001 Å and the break of the self-consistent loops was fixed to 10^{-8} eV.

Supporting Information

Supporting Information is available from the Wiley Online Library or from the author.

Conflict of Interest

The authors declare no conflict of interest.

[1] J. Greeley, T. F. Jaramillo, J. Bonde, I. Chorkendorff, J. K. Nørskov, *Nat. Mater.* **2006**, *5*, 909.

[2] D. Voiry, J. Yang, M. Chhowalla, *Adv. Mater.* **2016**, *28*, 6197.

[3] H. Jin, C. Guo, X. Liu, J. Liu, A. Vasileff, Y. Jiao, Y. Zheng, S.-Z. Qiao, *Chem. Rev.* **2018**, *118*, 6337.

[4] D. Deng, K. S. Novoselov, Q. Fu, N. Zheng, Z. Tian, X. Bao, *Nat. Nanotechnol.* **2016**, *11*, 218.

[5] A. Eftekhari, *J. Mater. Chem. A* **2017**, *5*, 18299.

[6] T. F. Jaramillo, K. P. Jorgensen, J. Bonde, J. H. Nielsen, S. Horch, I. Chorkendorff, *Science* **2007**, *317*, 100.

[7] M. R. Gao, M. K. Y. Chan, Y. Sun, *Nat. Commun.* **2015**, *6*, 8943.

[8] D. Kong, H. Wang, J. J. Cha, M. Pasta, K. J. Koski, J. Yao, Y. Cui, *Nano Lett.* **2013**, *13*, 1341.

[9] M. A. Lukowski, A. S. Daniel, F. Meng, A. Forticaux, L. Li, S. Jin, *J. Am. Chem. Soc.* **2013**, *135*, 10274.

[10] Y. Chen, A. Lu, P. Lu, X. Yang, C. Jiang, M. Mariano, B. Kaehr, O. Lin, A. Taylor, I. D. Sharp, L. Li, S. S. Chou, V. Tung, *Adv. Mater.* **2017**, *29*, 1703863.

[11] Y. Wan, Z. Zhang, X. Xu, Z. Zhang, P. Li, X. Fang, K. Zhang, *Nano Energy* **2018**, *51*, 786.

[12] H. Li, D. Minshu, M. J. Mleczko, A. L. Koh, Y. Nishi, E. Pop, A. J. Bard, X. Zheng, *J. Am. Chem. Soc.* **2016**, *138*, 5123.

[13] H. Li, C. Tsai, A. L. Koh, L. Cai, A. W. Contryman, A. H. Fragapane, J. Zhao, H. S. Han, H. C. Manoharan, F. Abild-Pedersen, J. K. Nørskov, X. Zheng, *Nat. Mater.* **2016**, *15*, 48.

[14] G. Gao, Q. Sun, A. Du, *J. Phys. Chem. C* **2016**, *120*, 16761.

[15] X. Chen, G. Wang, *Phys. Chem. Chem. Phys.* **2016**, *18*, 9388.

[16] D. Voiry, M. Salehi, R. Silva, T. Fujita, M. Chen, T. Asefa, V. B. Shenoy, G. Eda, M. Chhowalla, *Nano Lett.* **2013**, *13*, 6222.

[17] Y. Yin, J. Han, Y. Zhang, X. Zhang, P. Xu, Q. Yuan, L. Samad, X. Wang, Y. Wang, Z. Zhang, P. Zhang, X. Cao, B. Song, S. Jin, *J. Am. Chem. Soc.* **2016**, *138*, 7965.

[18] J. Xie, J. Zhang, S. Li, F. Grote, X. Zhang, H. Zhang, R. Wang, Y. Lei, B. Pan, Y. Xie, *J. Am. Chem. Soc.* **2013**, *135*, 17881.

[19] X. Zhou, Y. Liu, H. Ju, B. Pan, J. Zhu, T. Ding, C. Wang, Q. Yang, *Chem. Mater.* **2016**, *28*, 1838.

[20] D. Voiry, R. Fullon, J. Yang, C. de Carvalho Castro e Silva, R. Kappera, I. Bozkurt, D. Kaplan, M. J. Lagos, P. E. Batson, G. Gupta, A. D. Mohite, L. Dong, D. Er, V. B. Shenoy, T. Asefa, M. Chhowalla, *Nat. Mater.* **2016**, *15*, 1003.

[21] Y. Zhou, J. L. Silva, J. M. Woods, J. V. Pondick, Q. Feng, Z. Liang, W. Liu, L. Lin, B. Deng, B. Brena, F. Xia, H. Peng, Z. Liu, H. Wang, C. M. Araujo, J. J. Cha, *Adv. Mater.* **2018**, *30*, 1706076.

[22] D. Pierucci, H. Henck, J. Avila, A. Balan, C. H. Naylor, G. Patriarche, Y. J. Dappe, M. G. Silly, F. Sirotti, A. T. C. Johnson, M. C. Asensio, A. Ouerghi, *Nano Lett.* **2016**, *16*, 4054.

[23] R. K. Biroju, D. Das, R. Sharma, S. Pal, L. P. L. Mawlong, K. Bhorkar, P. K. Giri, A. K. Singh, T. N. Narayanan, *ACS Energy Lett.* **2017**, *2*, 1355.

[24] X. Han, X. Tong, X. Liu, A. Chen, X. Wen, N. Yang, X. Y. Guo, *ACS Catal.* **2018**, *8*, 1828.

[25] J. Ryou, Y. S. Kim, K. C. Santosh, K. Cho, *Sci. Rep.* **2016**, *6*, 29184.

[26] Y. Li, H. Wang, L. Xie, Y. Liang, G. Hong, H. Dai, *J. Am. Chem. Soc.* **2011**, *133*, 7296.

[27] M. R. Gao, J. X. Liang, Y. R. Zheng, Y. F. Xu, J. Jiang, Q. Gao, J. Li, S. H. Yu, *Nat. Commun.* **2015**, *6*, 5982.

[28] X. Dai, K. Du, Z. Li, H. Sun, Y. Yang, W. Zhang, X. Zhang, *Int. J. Hydrogen Energy* **2015**, *40*, 8877.

[29] P. Zhu, Y. Chen, Y. Zhou, Z. Yang, D. Wu, X. Xiong, F. Ouyang, *Int. J. Hydrogen Energy* **2018**, *43*, 14087.

[30] Y. Zhou, H. Jang, J. M. Woods, Y. Xie, P. Kumaravadivel, G. A. Pan, J. Liu, Y. Liu, D. G. Cahill, J. J. Cha, *Adv. Funct. Mater.* **2017**, *27*, 1605928.

[31] J. M. Woods, J. Shen, P. Kumaravadivel, Y. Pang, Y. Xie, G. A. Pan, M. Li, E. I. Altman, L. Lu, J. J. Cha, *ACS Appl. Mater. Interfaces* **2017**, *9*, 23175.

[32] S. Y. Lee, U. J. Kim, J. Chung, H. Nam, H. Y. Jeong, G. H. Han, H. Kim, H. M. Oh, H. Lee, H. Kim, Y. G. Roh, J. Kim, S. W. Hwang, Y. Park, Y. H. Lee, *ACS Nano* **2016**, *10*, 6100.

[33] M. J. Mleczko, R. L. Xu, K. Okabe, H. H. Kuo, I. R. Fisher, H. S. P. Wong, Y. Nishi, E. Pop, *ACS Nano* **2016**, *10*, 7507.

[34] C. Tsai, H. Li, S. Park, J. Park, H. S. Han, J. K. Nørskov, X. Zheng, F. Abild-Pedersen, *Nat. Commun.* **2017**, *8*, 15113.

[35] J. Wang, M. Yan, K. Zhao, X. Liao, P. Wang, X. Pan, W. Yang, L. Mai, *Adv. Mater.* **2017**, *29*, 1604464.

[36] D. R. Cummins, U. Martinez, A. Sherehiy, R. Kappera, A. Martinez-Garcia, R. K. Schulze, J. Jasinski, J. Zhang, R. K. Gupta, J. Lou, M. Chhowalla, G. Sumanasekera, A. D. Mohite, M. K. Sunkara, G. Gupta, *Nat. Commun.* **2016**, *7*, 11857.

[37] Y. Lin, X. Ling, L. Yu, S. Huang, A. L. Hsu, Y. H. Lee, J. Kong, M. S. Dresselhaus, T. Palacios, *Nano Lett.* **2014**, *14*, 5569.

[38] H. Liu, H. Kondo, T. Ohno, *Phys. Rev. B* **2012**, *86*, 155434.

[39] T. Cusati, G. Fiori, A. Gahoi, V. Passi, M. C. Lemme, A. Fortunelli, G. Iannaccone, *Sci. Rep.* **2017**, *7*, 5109.

[40] K. Nagashio, T. Nishimura, K. Kita, A. Toriumi, *Appl. Phys. Lett.* **2010**, *97*, 143514.

[41] S. M. Song, J. K. Park, O. J. Sul, B. J. Cho, *Nano Lett.* **2012**, *12*, 3887.

[42] A. Li, Y. Sun, T. Yao, H. Han, *Chem. - Eur. J.* **2018**, *24*, 18334.

[43] Z. Min, Y. Li, *J. Mater. Chem. A* **2015**, *3*, 14942.

[44] I. Niehues, R. Schmidt, M. Dru, P. Marauhn, D. Christiansen, M. Selig, G. Bergha, D. Wigger, R. Schneider, L. Braasch, R. Koch, A. Castellanos-gomez, T. Kuhn, A. Knorr, E. Malic, M. Rohl, R. Bratschitsch, *Nano Lett.* **2018**, *18*, 1751.

[45] W. Wu, J. Wang, P. Ercius, N. C. Wright, D. M. Leppert-simenauer, R. A. Burke, M. Dubey, A. M. Dogare, M. T. Pettes, *Nano Lett.* **2018**, *18*, 2351.

[46] Z. Dai, L. Liu, Z. Zhang, *Adv. Mater.* **2019**, 1805417.

[47] D. Voiry, H. Yamaguchi, J. Li, R. Silva, D. C. B. Alves, T. Fujita, M. Chen, T. Asefa, V. B. Shenoy, G. Eda, M. Chhowalla, *Nat. Mater.* **2013**, *12*, 850.

[48] X. Li, W. Liu, M. Zhang, Y. Zhong, Z. Weng, Y. Mi, Y. Zhou, M. Li, J. J. Cha, Z. Tang, H. Jiang, X. Li, H. Wang, *Nano Lett.* **2017**, *17*, 2057.

[49] W. Liu, E. Hu, H. Jiang, Y. Xiang, Z. Weng, M. Li, Q. Fan, X. Yu, E. I. Altman, H. Wang, *Nat. Commun.* **2016**, *7*, 10771.

[50] B. E. Conway, B. V Tilak, *Electrochim. Acta* **2002**, *47*, 3571.

[51] N. Pentland, J. O. Bockris, E. Sheldon, *J. Electrochem. Soc.* **1957**, *104*, 182.

[52] Z. Cai, Y. Bi, E. Hu, W. Liu, N. Dwarica, Y. Tian, X. Li, Y. Kuang, Y. Li, X. Q. Yang, H. Wang, X. Sun, *Adv. Energy Mater.* **2018**, *8*, 1701694.

[53] X. Zou, Y. Zhang, *Chem. Soc. Rev.* **2015**, *44*, 5148.

[54] I. Roger, M. A. Shipman, M. D. Symes, *Nat. Rev. Chem.* **2017**, *1*, 0003.

[55] M. N. Ali, J. Xiong, S. Flynn, J. Tao, Q. D. Gibson, L. M. Schoop, T. Liang, N. Haldolaarachchige, M. Hirschberger, N. P. Ong, R. J. Cava, *Nature* **2014**, *514*, 205.

[56] Q. Ji, Y. Zhang, T. Gao, Y. Zhang, D. Ma, M. Liu, Y. Chen, X. Qiao, P. H. Tan, M. Kan, J. Feng, Q. Sun, Z. Liu, *Nano Lett.* **2013**, *13*, 3870.

[57] W. Zheng, T. Xie, Y. Zhou, Y. L. Chen, W. Jiang, S. Zhao, J. Wu, Y. Jing, Y. Wu, G. Chen, Y. Guo, J. Yin, S. Huang, H. Q. Xu, Z. Liu, H. Peng, *Nat. Commun.* **2015**, *6*, 7972.

[58] J. V. Pondick, J. M. Woods, J. Xing, Y. Zhou, J. J. Cha, *ACS Appl. Nano Mater.* **2018**, *1*, 5655.

[59] Y. Zhu, Y. Li, G. Arefe, R. A. Burke, C. Tan, Y. Hao, X. Liu, X. Liu, W. J. Yoo, M. Dubey, Q. Lin, J. C. Hone, *Nano Lett.* **2018**, *18*, 3807.

[60] M. Payne, T. MP, D. Allen, T. Arias, J. Joannopoulos, *Rev. Mod. Phys.* **2011**, *64*, 1045.

[61] R. O. Jones, O. Gunnarsson, *Rev. Mod. Phys.* **1989**, *61*, 689.

[62] W. Kohn, L. Sham, *PhysRev* **1965**, *140*, 1133.

[63] P. E. Blöch, *Phys. Rev. B* **1994**, *50*, 17953.

[64] G. Kresse, J. Furthmu, *Phys. Rev. B* **1996**, *54*, 11169.

[65] G. Kresse, D. Joubert, *Phys. Rev. B* **1999**, *59*, 1759.

[66] G. Kresse, J. Hafner, *Phys. Rev. B* **1993**, *48*, 13115.

[67] J. P. Perdew, K. Burke, M. Ernzerhof, *Phys. Rev. Lett.* **1997**, *78*, 1396.

[68] S. Grimme, *J. Comput. Chem.* **2006**, *27*, 1787.

[69] J. D. Pack, H. J. Monkhorst, *Phys. Rev. B* **1977**, *16*, 1748.